NUMERICAL SIMULATION OF SEDIMENT ENTRAINMENT BY LOCK-EXCHANGE GRAVITY CURRENTS

FOTEINI KYROUSI[(1)], ALESSANDRO LEONARDI[(2)], CARMELO JUEZ[(3)], JESSICA ZORDAN[(4)], FRANCESCA ZANELLO[(5)], FEDERICO ROMAN[(6)], VINCENZO ARMENIO[(7)] & MÁRIO J. FRANCA[(8)]

[(1,2,5)]Idrostudi Srl, Area di Ricerca, Trieste, Italy
foteini.kyrousi@phd.units.it
[(3,4,7,8)]Department of Engineering and Architecture, University of Trieste, Italy
[(6)]Laboratoire de Constructions Hydrauliques, École polytechnique fédérale de Lausanne, Switzerland
[(4)]Iefluids S.r.l., Trieste, Italy

ABSTRACT

Gravity currents are flows driven by buoyancy differences between two contacting fluids caused by differences in temperature, salinity, or by the presence of suspended particles. Such flows can reach high velocities near the bed, especially on the area behind the front of the current. As a result, rapid morphological changes may take place in river and estuarine beds due to the passage of these flows. Essential to determine the erosion induced by the current, are the spatial and temporal distributions of the bed shear stress. However, these are troublesome to measure in laboratory or in the field. To bridge this difficulty, the eddy-solving numerical simulations may be used. This study presents here the three-dimensional numerical simulations of lock-exchange salinity currents flowing over a mobile bed. It is aimed at the characterization of the sediment entrainment capacity of the current. The large eddy simulation technique is employed for analyzing the evolution and the structure of the current. For the sediment simulation, an Euler-Euler methodology based on a single phase approach is used. The main features of the current are compared with experimental data obtained in the laboratory. Velocity fields and bed shear stress distributions for different initial current densities are analyzed and linked to entrainment scenarios. The influence of small variations in particle size of the mobile bed is also discussed.

Keywords: Gravity current; large Eddy simulations (LES); suspended sediment transport; sediment erosion.

1 INTRODUCTION

The propagation of gravity currents, triggered by the release of a heavier fluid in a less dense water body, can cause, among other phenomena, important environmental impacts such as rapid morphological changes in river and estuarine beds, reservoir sedimentation, damages in submarine emissaries and cables, and pollutant dispersion. All of this makes their understanding of prime interest in environmental sciences. Gravity currents can be formed in many different natural situations. They can be caused by natural events e.g., sea breeze fronts, oceanic overflow, avalanches and volcanic eruption; or by anthropogenic activities e.g. accidental release of a dense gas, oil spillages or pollutant discharge in water bodies (Simpson, 1997).

Due to the unpredictable nature of such flows and to technical difficulties, field studies are quite limited. Hence, our understanding on the dynamics of gravity currents is based mainly on laboratory experiments and high-resolution simulations. The numerical tools that have been mainly used over the last years to study the behavior of gravity currents are Direct Numerical Simulations (DNS), that resolves all the relevant scales in the flow down to the dissipative range, and Large Eddy Simulations (LES), where a subgrid-scale model is used instead of resolving the smaller scales. In particular, pioneering DNS for density-driven gravity currents in low Reynolds number were presented by Härtel et al. (2000a; 2000b) and Necker et al. (2002). However, DNS is restricted mainly to low Reynolds number flows and simple geometries due to its computational cost, whereas LES has proven useful on high Reynolds number flows over complex geometries. Gravity currents with high Reynolds number, its effects on the bed shear stress distribution, and its interaction with obstacles, were investigated using LES by Ooi et al. (2009), Gonzalez-Juez et al. (2009) and Tokyay et al. (2011).

Gravity currents have the capacity to erode a loose bed, if they are fast enough so that the bed shear stress exceeds the threshold of motion of the bed material (see Figure 1). The sedimentation induced by turbidity currents has been extensively investigated in literature (Akiyama et al., 1985; Eames et al. (2001); Necker et al., 2002; Blanchette et al., 2005). However, to the best of our knowledge, few studies (Garcia and Parker, 1991) focused on the lift-off mechanisms and the distribution of the entrained material in the body of the current. To study the particle entrainment induced by gravity currents requires detailed, spatial and temporal, measurements of velocities, bed shear stress distribution and sediment concentration. The purpose of the present work is to investigate numerically the capacity of salinity current to bring bed material into suspension. For this purpose, the LES of compositional gravity currents is performed in lock-exchange configuration, flowing over a channel reach where the bed is mobile. Different buoyancy Reynolds numbers of

the current and different grain size of the bed particles are tested. The change of particle diameters is modeled by changing the critical Shields number and the settling velocity. The density gradient is given by a salinity difference between the heavier and the ambient fluid, which is small enough for the Boussinesq approximation to be valid. The initial aspect ratio of the lock fluid, *R*, is large ($R = {}^{H}/_{x_0} \ll 1$, where H is the water depth and x_0 is the distance between the lock and the rear wall), and this study considers a full-depth release. The governing equations of the flow are numerically integrated using LES-COAST, an unsteady Navier-Stokes solver, written under the Boussinesq approximation and based on the work in Zang et al. (1994). The sub-grid scale (SGS) terms have been modeled using a Smagorinsky dynamic Lagrangian model (Meneveau et al., 1996). Both salinity and sediment concentration are considered as active scalars and an Euler-Euler approach has been employed, which considers the two phases as a mixture. The numerical results provide a detailed description of the salinity current, the comparison of its main features with experimental results provided by Zordan et al. (2017). LES supplies information on the velocity and density fields, the spatial and temporal distribution of the bed shear stress exactly before the erodible section of bed, and the evolution of the sediment concentration above the mobile bed.

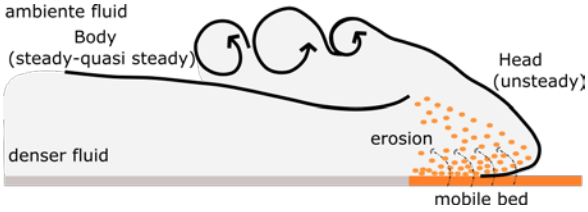

Figure 1. Sketch of a gravity current propagation and entraining and bed sediment.

The article is organized as follows: First the case that this paper is planning to study is described along with the illustration of the mathematical and numerical model. Sec. 4 presents the main characteristics of the current and their comparison with experimental data, while the results for the velocity field and the estimation of bed shear stress are discussed in Sec. 5. The contours of entrained sediment concentration are analyzed in Sec. 6 followed by a brief summary and the main conclusions.

2 DESCRIPTION OF THE STUDY CASE

The geometry used in this work was inspired by the experimental configuration described in Zordan et al. (2017). A sketch description of the experimental set-up is given in Figure 2. The flume used in the experiments was *7.48* m long, *0.275* m wide and was filled at both sides of the gate up to a depth of *H=0.2* m. Downstream of the horizontal flume the current dissipates in a large tank. The horizontal flume was separated by a movable lock-gate at a distance $x_0 = 2.5$m from the rear wall. At each side of the gate, volumes of fluid with different densities were contained. The fluid volume behind the lock had an initial salinity equal to C^1_{sal} and density ρ_{lock} (see Table 1), while the fluid volume beyond the lock had a zero-initial salinity C^0_{sal}*=0* kg/m^3 and the density of clear water ρ_w. Density is connected to salinity by the state equation shown hereafter (Eq. 1), where β is the salinity contraction coefficient whose value can be found in UNESCO/IOC et al. 2010.

$$\rho = \rho_w[1 + \beta(C_{\mathrm{sal}} - C^0_{\mathrm{sal}}] \qquad [1]$$

The apparatus simulates the classical lock exchange gravity current (Nogueira et al. 2013; Theiler and Franca, 2016). When the gate is removed, the heavier fluid starts flowing towards the bottom of the flume creating a current that flows away from the gate, while the lighter fluid is displaced creating a counter current that protrudes on top of the heavier fluid. As a consequence, between the two fluids a shear layer forms, which provokes mixing due to Kevin-Hemholtz instabilities.

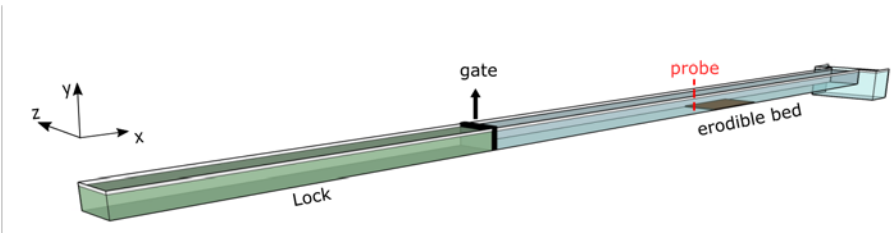

Figure 2. Lock-exchange configuration corresponding to the experiments by Zordan et al. (2017) which has inspired the numerical set-up. The volume indicated by green color represents the heavier fluid, while the volume with the blue color indicates the lighter fluid. The erodible section of the bed is shown by brown color. The red dashed line demonstrates the position of the probe where the numerical measurements are collected.

The fluid density on the two sides of the lock-gate is very similar (they do not exceed *O* (1%)), and the Boussinesq hypothesis is valid. Four different simulations are performed using two different values for the initial salinity C^1_{sal} and changing the bed material characteristics, such as critical Shields parameter, θ_{cr} and settling velocity, w_s. The numerical parameters for the different runs are reported in Table1.

The buoyancy Reynolds number, Re_b, and the Froude number, *Fr*, are defined as,

$$\text{Re}_b = \frac{u_b H}{v}, \quad [2]$$

$$\text{Fr} = \frac{u_{front}}{u_b}, \quad [3]$$

where *v* is the molecular viscosity, u_{front} is the velocity of the current front at the slumping phase and u_b is defined as,

$$u_b = \sqrt{g' H}, \quad [4]$$

where

$$g' = g\,\frac{\rho_{\text{lock}} - \rho_w}{\rho_w}. \quad [5]$$

Table 1. Parameters of lock-exchange numerical simulations.

	ρ_{lock} (kg/m^3)	C^1_{sal} (psu)	g' (m/s^2)	u_b (m/s)	u_{front} (m/s)	Re_b	Fr	θ_{cr}	w_s
A	1030	40	0.294	0.2426	0.109	48991	0.449	0.25	5.5x 10^{-4}
B	1030	40	0.294	0.2426	0.109	48991	0.449	0.17	13.7 x10^{-4}
C	1040	53	0.392	0.2801	0.117	55961	0.417	0.25	5.5x 10^{-4}
D	1040	53	0.392	0.2801	0.117	55961	0.417	0.17	13.7 x10^{-4}

3 MATHEMATICAL MODEL AND NUMERICAL SET-UP

3.1 Governing equations and numerical method

The dynamics of the gravity current obey the Navier-Stokes equations for incompressible flows, in the form given by the Boussinesq approximation for the buoyancy effects. The momentum and mass conservation equations are also coupled with two scalar transport equations: one for the salinity and one for the sediment concentration. In the Navier-Stokes equations, the influence of the density variations due to salinity and sediment concentration is taken into account through additional forcing terms in the vertical momentum conservation. The LES-filtered continuity equation, momentum equation, and the two scalar transport equations have been scaled using the buoyancy velocity of the current u_b and the water depth H as follows:

$$\frac{\partial \bar{u}_i}{\partial x_i} = 0, \quad [6]$$

$$\frac{\partial \bar{u}_i}{\partial t} + \frac{\partial \bar{u}_j \partial \bar{u}_i}{\partial x_j} = -\frac{\partial \bar{p}}{\partial x_i} + \frac{1}{\text{Re}_\text{b}} \frac{\partial^2 \bar{u}_i}{\partial x_j \partial x_j} - \frac{\Delta \hat{\rho}}{\rho_{\text{lock}} - \rho_\text{w}} \delta_{i,j=2} - \frac{\partial \tau_{ij}}{\partial x_j}, \quad [7]$$

$$\frac{\partial \bar{C}_{\text{sal}}}{\partial t} + \frac{\partial \bar{u}_j \bar{C}_{\text{sal}}}{\partial x_j} = \frac{1}{\text{Re}_\text{b}\text{Sc}_{\text{sal}}} \frac{\partial^2 \bar{C}_{\text{sal}}}{\partial x_j \partial x_j} - \frac{\partial \lambda_j}{\partial x_j}, \quad [8]$$

$$\frac{\partial \bar{C}_{\text{sed}}}{\partial t} + \frac{\partial (\overline{u}_{j-w_s \delta_{i2}}) \bar{C}_{\text{sed}}}{\partial x_j} = \frac{1}{\text{Re}_\text{b}\text{Sc}_{\text{sed}}} \frac{\partial^2 \bar{C}_{\text{sed}}}{\partial x_j \partial x_j} - \frac{\partial \eta_j}{\partial x_j}. \quad [9]$$

In the equations above, $\bar{p}$ represents the filtered pressure and $\bar{u}_i$ the filtered velocity vector where i represents the x, y and z directions of the computational domain. $\delta_{i,j=2}$ is a unit vertical vector against gravity, w_s is the settling velocity of the particles, and Sc_{sal} and Sc_{sed} indicate the Schmidt number of salt and sediments concentration, equal to *600* and *1*, respectively. The effect of the small-scale diffusion in the momentum equations (Eq. 7) appears as additional SGS stresses τ_{ij}, defined by:

$$\tau_{ij} = -2\nu_\text{t} \bar{S}_{ij}, \quad [10]$$

where ν_t denotes the SGS eddy viscosity. The additional salinity and concentration SGS fluxes λ_i andη_i appearing in the scalar transport equation are defined by:

$$\lambda_j = -\frac{\nu_\mathrm{t}}{\mathrm{Sc}^\mathrm{t}_\mathrm{sal}}\frac{\partial \bar{C}_\mathrm{sal}}{\partial x_j}, \quad [11]$$

$$\eta_j = -\frac{\nu_\mathrm{t}}{\mathrm{Sc}^\mathrm{t}_\mathrm{sed}}\frac{\partial \bar{C}_\mathrm{sed}}{\partial x_j}, \quad [12]$$

with $\mathrm{Sc}^\mathrm{t}_\mathrm{sal}$and $\mathrm{Sc}^\mathrm{t}_\mathrm{sed}$ denoting the SGS Schmidt numbers. The SGS quantities are calculated using the Lagrangian dynamic model introduced by Meneveau et al. (1996).
The density variation due to gradients in salinity and sediments is equal to:

$$\frac{\Delta\hat{\rho}}{\rho_\mathrm{lock}-\rho_\mathrm{w}} = \frac{\rho-\rho_\mathrm{w}}{\rho_\mathrm{lock}-\rho_\mathrm{w}} = \frac{\bar{C}_\mathrm{sal}}{\bar{C}^1_\mathrm{sal}} + \frac{s}{\beta\bar{C}^1_\mathrm{sal}}\bar{C}_\mathrm{sed}, \quad [13]$$

with s the sediment buoyant density:

$$s = \frac{\rho_\mathrm{sed}-\rho_\mathrm{w}}{\rho_\mathrm{w}}. \quad [14]$$

3.2 Sediment parameters

When the gravity current passes over the mobile bed, particles can be eroded and brought into suspension. Following the typical approach, it is here assumed that the erosion of sediments begins only when the dimensionless bed shear stress, θ exceeds a critical value. This critical valueθ_cr has been determined using the model for suspended sediments of Vanoni (1975), in turn based on the seminal work by Shields (1936). The erosion rate is calculated using the pick-up function proposed by Luque et al. (1976) which yields to good results for small particle sizes (<*200*μm), (Van Rijn, 1984):

$$E = a\rho_\mathrm{sed}(sgd_\mathrm{sed})^{0.5}(\theta-\theta_\mathrm{cr})^{1.5}, \quad [15]$$

where $a = 0.02$ for spherical particles, d_sed is the sediment diameter and θ represents the Shields parameter equal to $\frac{\tau_\mathrm{w}}{sg\rho_\mathrm{w}d_\mathrm{sed}}$.

The settling velocity of the suspended sediments is one of the key parameters to characterize their behavior. In this work, the particles are cohesionless and have a mean diameter d in the range from *75* to *150*μm. For this particle range size, there are many different formulations for calculating the settling velocity. Here, the approach proposed by Zanke (1977) was chosen, for its simplicity (Eq. 16).

$$w_\mathrm{s} = \frac{10\nu}{d_\mathrm{sed}}\left[\left(1+\frac{0.01sgd_\mathrm{sed}{}^3}{\nu^2}\right)^{0.5}-1\right]. \quad [16]$$

3.3 Numerical set up and boundary conditions

The 3D code LES-COAST developed at the University of Trieste was used to simulate the gravity current and the particle entrainment. A detailed discussion of the governing equations and their spatial and temporal discretization is provided in Armenio and Sarkar, (2002). The code has been widely tested in the past for similar cases (Dallali and Armenio, 2015). The spatial resolution of the domain is 1336x128x80 grid points in the streamwise (x), vertical (y) and spanwise (z) direction, respectively. Stretching has been applied in the vertical and spanwise directions, following Vinokur's algorithm (Vinokur, 1983), so that close to the bottom walls $\Delta y^+ = 1$ and close to the side walls $\Delta z^+ = 1$ at the first grid point. This discretization satisfies the requirements for wall-resolved LES, and no further wall model is required.
In the simulations, the bottom and side surfaces are modeled as no-slip smooth walls, while the top free-surface condition is approximated using a free-slip condition. The presence of the tank is simulating numerically by a downstream extension of the numerical domain. Zero salinity fluxes are imposed at all boundaries. Concerning the sediment concentration, on the top surface the mass exchange is assumed to be equal to zero:

$$\frac{1}{Re_\mathrm{b}Sc_\mathrm{sed}}\frac{\partial \bar{C}_\mathrm{sed}}{\partial y} + w_\mathrm{s}\bar{C}_\mathrm{sed} = 0. \quad [17]$$

At the bottom, the mass exchange is a function of the particle erosion E and deposition S rates, given by:

$$\left(\frac{1}{Re_{\mathrm{b}}Sc_{\mathrm{sed}}}\frac{\partial \bar{C}_{\mathrm{sed}}}{\partial y}+w_{\mathrm{s}}\bar{C}_{\mathrm{sed}}\right)\cdot \boldsymbol{n}=S(\boldsymbol{n}\cdot\delta_{i2})-\frac{E}{\rho_{\mathrm{sed}}}, \qquad [18]$$

where $\boldsymbol{n}$ is a unit vector normal to the sediment surface. Erosion rate, *E*, is imposed equal to zero everywhere except on the mobile section of the bed. The sedimentation rate of the particles is defined as:

$$S=w_{\mathrm{s}}c_{\mathrm{ref}}, \qquad [19]$$

in which c_{ref} refers to the sediment concentration at the vicinity of the wall, chosen to be equal to the concentration of the first grid point away from the wall.

4 DESCRIPTION OF THE CURRENT

The main focus of this section is to study the main features of the salinity current. In this regard, two density currents with different buoyancy Reynolds numbers are simulated (case A and C). The Reynolds numbers are chosen to be equal to those used by Zordan et al. (2017). Being the experiments analogous to simulations A and C, they will be referred to as A_{exp} and C_{exp} in the following.

The behavior of the current is comparable to similar results found in literature. Figure 3 shows the spanwise-averaged density field obtained from simulation A. These results are in accordance with those described in Constantinescu (2014) for high-buoyancy Reynolds numbers. More specifically, the flow is strongly turbulent behind the front, and the billows lose their coherence after a short time. A stable stratification over a slightly tilted layer can be observed at a distance from the front.

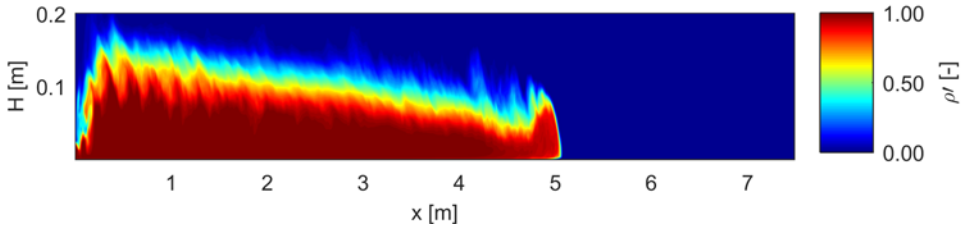

Figure 3. Simulations A: spanwise-averaged dimensionless density contour illustrating the propagation of the current for case A at time $t = 23t_0$. ρ' represents the dimensionless density field equal to $\frac{\rho-\rho_w}{\rho_{lock}-\rho_w}$.

For case A, the evolution of the front position of the current with respect to the lock-gate is calculated numerically and compared with experimental data obtained by the experimental work of Zordan et al. (2017). It is worth noting that during the slumping phase, the velocity of the front is roughly constant, which allows the head of the front to be examined under quasi-steady conditions (Härtel et al, 2000a). The front velocity is measured indirectly by recording the time evolution of the front location, which is defined as the position of the nose of the current in the streamwise direction at a height of *2*mm from the bed. Simulations can provide the whole record of the front location. However, experimentally the position of the front is recorded only above the mobile section of the bed. The front location with respect to the gate position measured for A and A_{exp} is shown in Figure 4. A very good agreement for the front velocity becomes evident comparing the slopes of the lines. Moreover, these results illustrate that in case A, the presence of suspended sediments does not alter the current dynamics. This subject is discussed in details in the next Section.

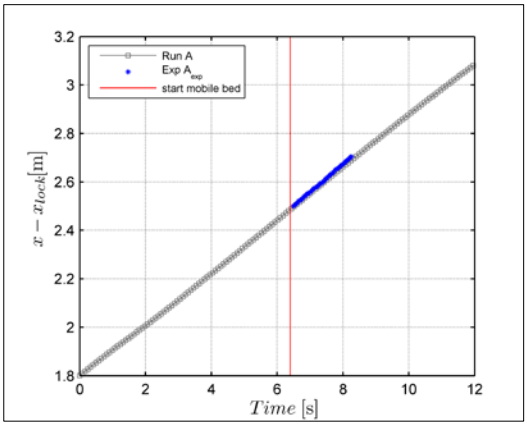

Figure 4. Time evolution of the front position, with respect to the lock gate, for numerical case A and experimental case A_{exp}. The red vertical line represents the time instant when the current reaches the mobile bed.

The shape of the current at a given location also serves as a good validation criterion (Constantinescu, 2014). Thus, an accurate depiction of the current shape must consider the interface between current and counter-current. This interface, however, cannot be obtained directly from A_{exp} and C_{exp} because density measurements are not available. Nevertheless, by evocating the following assumptions: (1) frozen turbulence hypothesis hold true (Parsons and Garcia, 1998), and (2) the interface of the gravity current is conserved along streamlines, it is considered that the current is advected by a constant velocity equal to the velocity of the front. In this regard, time series of velocities measurements can be used as means of retrieving the shape of the gravity current. It is believed that the inflection point of the velocity profile roughly coincides with the interface between the denser and the lighter fluids; that is where the velocity changes sign. Note however that this velocity is chosen to be very close to zero, as choosing zero is too general and not measurable in practice. The outcomes of the numerical simulations A and C are compared with the experimental results Aexp and Cexp. The velocity measurements used in the present work have been taken along the vertical axis at a probe located at the same distance from the lock as in Zordan et al. (2017). This is just before the mobile bed, and erosion has not started yet. A direct comparison between experimental and numerical data is given in Figure 5. The velocity measurements at the present work have been taken along the vertical at a probe located at the entrance of the mobile bed. From the plot, it is clear that during the first 7 seconds the head of the current, where most of the mixing and dynamics occurs, passes through the probe. After the head, the remaining part of the denser fluid, which is carried inertially, passes. Numerical and experimental results show very good agreement.

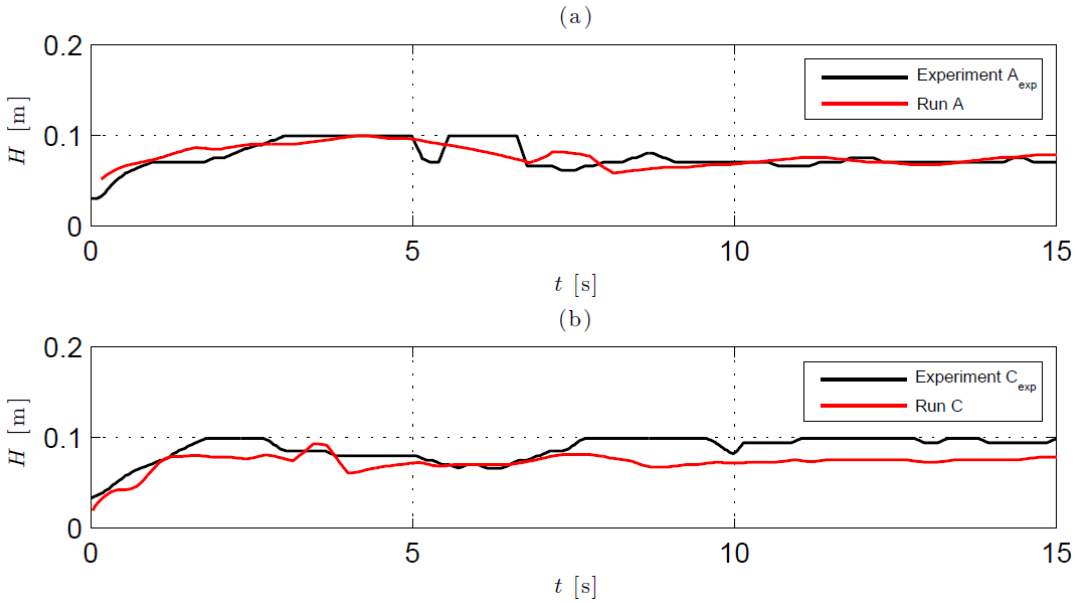

Figure 5. Current shape simulated in run A and C compared with the recorded in the laboratory experiments A_{exp} and C_{exp}, respectively. Plot (a) represents simulation A and experiment A_{exp}, while plot (b) represents simulation C and experiment C_{exp}.

5 VELOCITY PROFILES AND BED SHEAR STRESS

The instantaneous streamwise velocity contours for runs A and C, measured at a probe located at the half width of the channel at the entrance of the mobile bed are shown in Figure 6. In the same figure, the solid line represents the time series of the bed shear stress measured in the same location. The results indicate that the portion with the highest erosive power is, as expected, located at the front of the current. This relates to the region of high shear in the interface of the billow with the ambient fluid where most instabilities of the cleft-lobe type occur. The high-shear region, however, does not present a homogeneous structure in the spanwise direction. In accordance to Ooi et al. (2009), the regions of high bed shear show the emergence of elongated streamwise streaks of high/low shear.

In the current, this happens below head and billow. These streaks are responsible of the saltation and suspension mechanisms found on loose bed hydraulics. In the billow behind the head, a sudden decrease in bed shear is seen instead. The time series of bed shear stress at different spanwise locations is shown in Figure 7. Section $z1$ corresponds to the mid-spanwise probe, while section z_2 is located at distance ¼ z from the lateral wall. The high variation of τ that is observed between sections $z_1$and z_2 may be also an indication of the presence of such streaks.

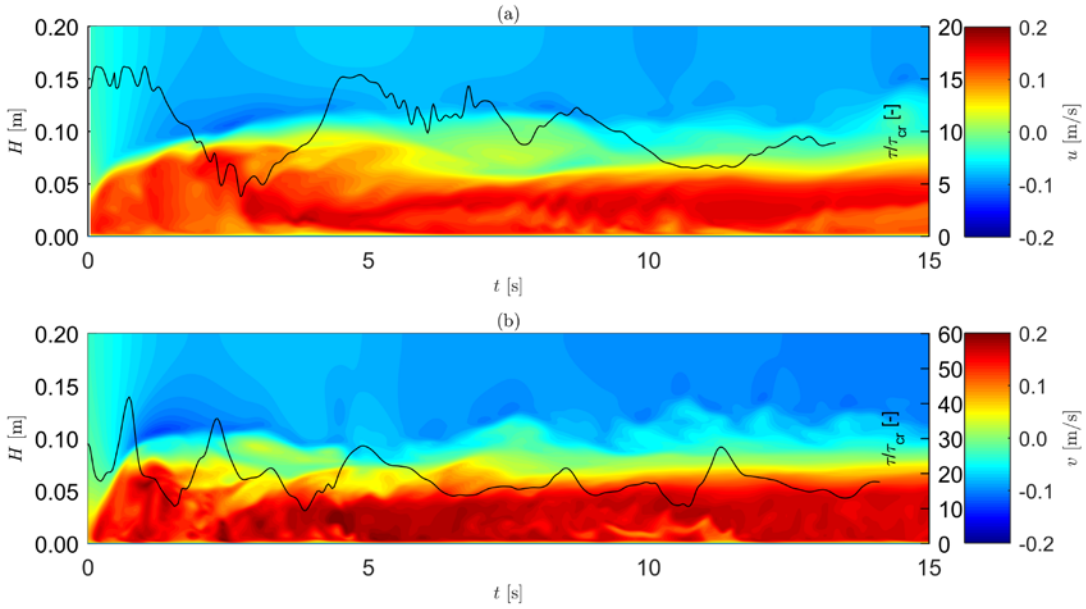

Figure 6. Streamwise velocity contours and bed shear stress evolution on a specific probe in the mid-spanwise section, (a) represents run A, (b) represents run C.

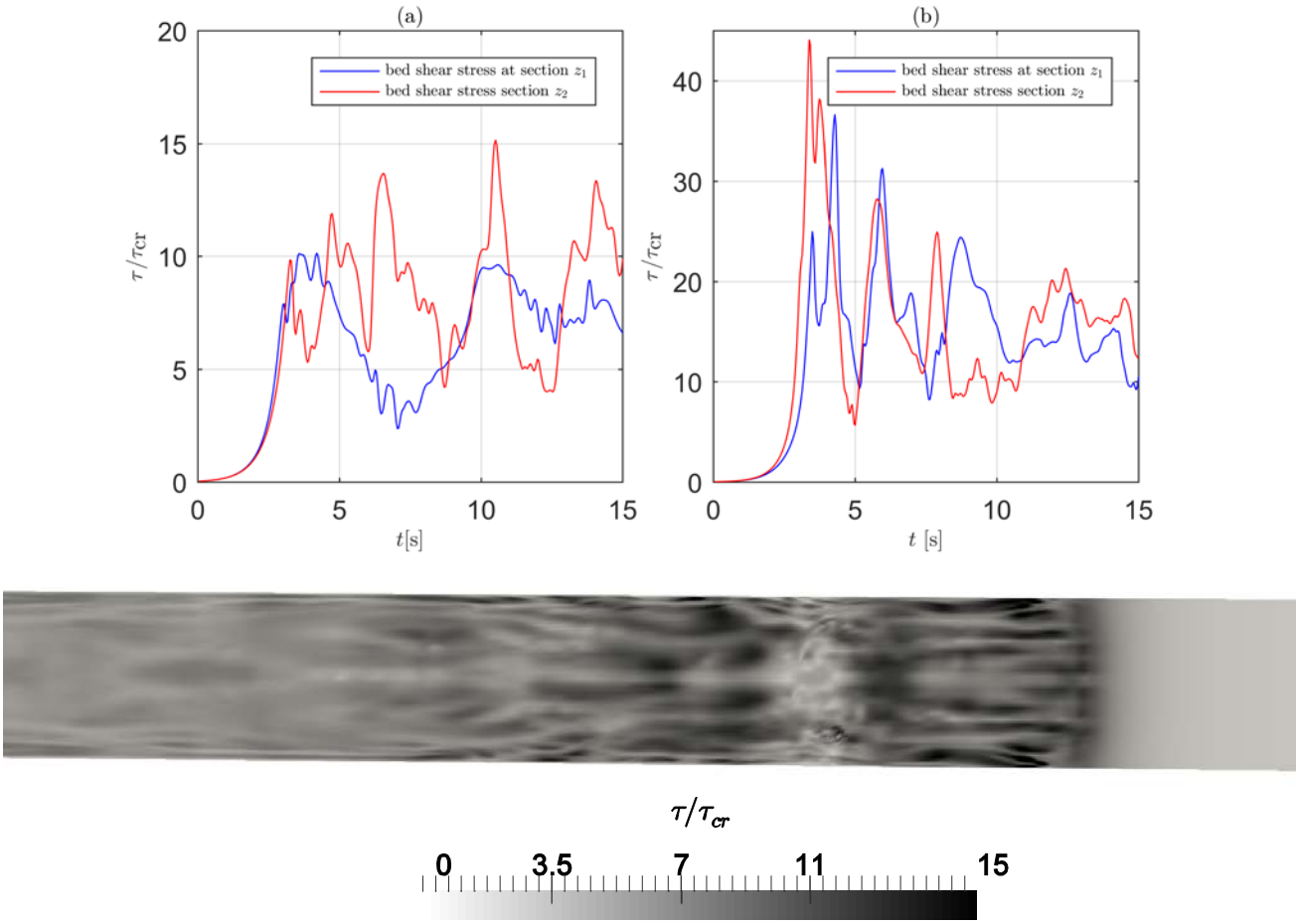

Figure 7. Time and space evolution of the dimensionless bed shear stress. Section z_1 corresponds to the mid-spanwise probe, while section z_2 is located at distance ¼ z from the lateral wall. Plot (a) represents the time evolution for simulation A, plot (b) represents the time evolution for simulation C, and plot (c) represents the space evolution of bed shear stress for simulation A.

6 SEDIMENT ENTRAINMENT

The previous sections argued that most of the sediment entrainment originating from the mobile bed should come from the front of the current, which carries most of the erosive energy. Four different simulations are performed (see Table 1) in order to study the capacity to entrain particles. In Figure 8, the spanwise

averaged sediment concentration, $\langle c \rangle$, contours for the various entrainment scenarios are shown. In particular, Figure 8a and 8b represent simulations A and B respectively, where the buoyancy Reynolds number is constant ($Re_{\mathrm{b}} = 48991$), but different particle diameters are used for the erodible section of the bed. These diameters are chosen within the range of applicability of the pick-up function described with Eq. 15 and also different enough to study the forces causing entrainment and suspension. More specifically, changing the particle diameter influences the Shields parameter θ_{cr} in Eq. 15 and the settling velocity w_{s} in Eq. 16. Decreasing the particle diameter, particle entrainment increases, as expected. However, the suspension is restricted behind the front and drops to almost zero in the body of the current. The total sediment concentration in the flow is quite low, *O* (0.001%). That means that, in cases A and B, the suspended sediments can be considered passive without visibly influencing the current dynamics. For this reason, as it has been observed in previous section, the front velocity of the current does not change significantly due to the presence of the mobile bed.

(a). Simulation A

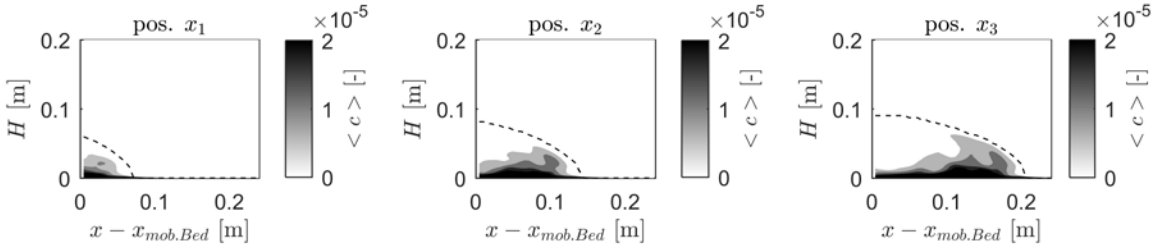

(b). Simulation B

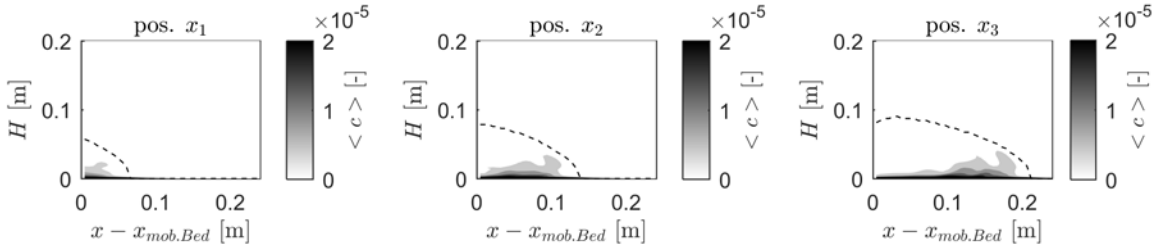

(c). Simulation C

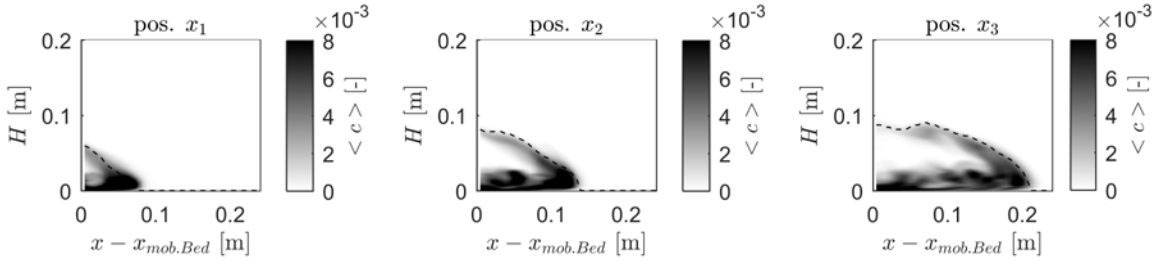

(d). Simulation D

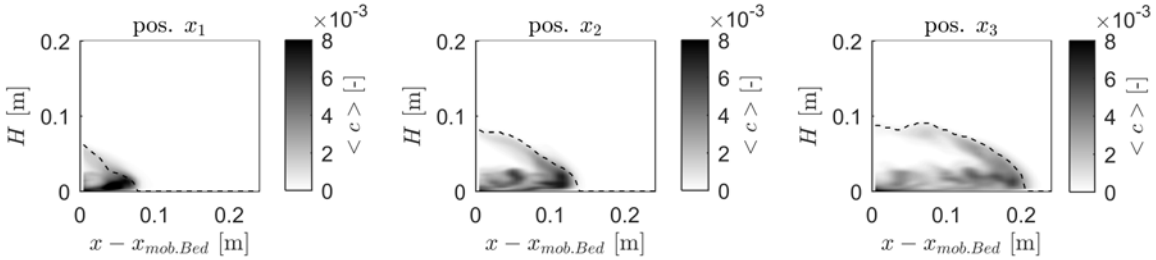

Figure 8. Visualization of the shape of the current (dashed line) and spanwise averaged sediment concentration $\langle c \rangle$ contours at different positions above the mobile bed. The shape of the current is identified by choosing the iso-density contour $\frac{\rho - \rho_w}{\rho_{lock} - \rho_w} = 0.02$ as a threshold between the current and the ambient fluid, as proposed by Ottolenghi et al., 2016. (a) represents run A, (b) represents run B, (c) represents run C, and (d) represents run D.

For simulations C and D, presented in Figure 8c and 8d, the buoyancy Reynolds number of the current has been changed to $Re_{\mathrm{b}} = 55961$, and the same particle diameters mentioned above are tested. In this manner, this study discerns the role of turbulence in the transport of the particles. It is clear that the increase of the initial density difference leads to a current with higher erosive energy. This is also in agreement with the

graphs in Figure 7, where a substantial increase of the bed shear stress is observed by increasing the density of the current. Additionally, by increasing the turbulence, the sediments are able to travel higher in the body of the current C.

A general observation is that the suspended material takes a shape similar to that of the head recirculation which might imply some type of scale similarity and coherence between the flows. This trend, apparent in Figure 8, is an inverse function of the particle diameter and directly proportional to the density of the gravity current.

7 CONCLUSIONS

In this work, LES has been used to study the sediment entrainment capacity of salinity currents with large release volumes and characterized by high Reynolds numbers. In the first part of the paper, the simulation results taking into account different Reynolds number have been compared with experimental data by Zordan et al. (2017). Very good agreement between numerical output and experimental measurements has been obtained for both front velocity and shape of the current. In the second part, the numerical results have been analyzed and the dynamics of the currents have been discussed for what concerns velocities and bed shear distribution. Finally, the sediment entrainment for different cases has been presented. Presented results indicate that the flow behind the front of the current is strongly turbulent, which leads to high peaks of bed shear stress. However, the spatial bed shear stress distribution is not uniform behind the front. When the current passes over the mobile bed, the stress peaks are the main contributor to sediment entrainment, which in turn concentrates just behind the front. Furthermore, as it is expected that by increasing the density of the current, its capacity to entrain particles is also increased.

It is worth mentioning that the numerical results, regarding the particle entrainment, may change depending on the mathematical models that are chosen to reproduce erosion and the deposition of the particles. Further studies are needed to define the implications behind the choice of a specific model. Comparisons with experimental data would also be important for the validation of the numerical model regarding the sediment entrainment.

Finally, the dynamics of the current in general are also dependent on the bed forms that create during its passage. These should follow the spatial distribution of the bed shear stress. However, since the bed forms influence the current itself, the results might deviate consistently from those reported in this work. Hence, further effort should be devoted into clarifying this mechanism as well as to study the feedback of the suspended sediments in the current dynamics, as for example their influence on the front velocity of the current.

ACKNOWLEDGEMENTS

The research leading to these results has received funding from the People Programme (Marie Curie Actions) of the European Union's Seventh Framework Programme FP7/2007-2013/ under REA grant agreement n’ 607394-SEDITRANS. The authors are grateful to S. López Castaño for useful discussions. The experimental data can be made available upon request to J. Zordan and C. Juez.

REFERENCES

Akiyama, J. & Stefan, H. (1985). Turbidity Current with Erosion and Deposition. *Journal of Hydraulic Engineering,* 111(12), 1473-1496.

Armenio, V. & Sarkar, S. (2002). An Investigation of Stably Stratified Turbulent Channel flow using Large-Eddy Simulation. *Journal of Fluid Mechanics,* 459, 1-42.

Blanchette, F., Strauss, M., Meiburg, E., Kneller, B. & Glinsky, M. E. (2005). High-Resolution Numerical Simulations of Resuspending Gravity Currents: Conditions for Self-Sustainment. *Journal of Geophysical Research: Oceans,* 110(C12).

Constantinescu, G. (2014). LES of Lock-Exchange Compositional Gravity Currents: A Brief Review of Some Recent Results. *Environmental Fluid Mechanics,* 14(2), 295-317.

Dallali, M. & Armenio, V. (2015). Large Eddy Simulation of Two-Way Coupling Sediment Transport. Advances in Water Resources, 81, 33-44.

Eames, I., Hogg, A.J., Gething, S. & Dalziel, S.B. (2001). Resuspension by Saline and Particle-Driven Gravity Currents. *Journal of Geophysical Research,* 106(C7), 14095-14111

Garcia, M. & Parker, G. (1991). Entrainment of Bed Sediment into Suspension. *Journal of Hydraulic Engineering,* 117(4), 414-435.

Gonzalez-Juez, E., Meiburg, E. & Constantinescu, G. (2009). The Interaction of a Gravity Current with a Circular Cylinder Mounted above a Wall: Effect of the Gap Size. *Journal of Fluids and Structures,* 25(4), 629-640.

Härtel, C., Carlsson, F. & Thunblom, M. (2000b*).* Analysis and Direct Numerical Simulation of the Flow of a Gravity Current Head. *Journal of Fluid Mechanics,* 418, 213-229

Härtel, C., Meiburg, E. & Necker, F. (2000a). Analysis and Direct Numerical Simulation of the Flow at a Gravity-Current Head. Part 1: Flow Topology and Front Speed for Slip and No-Slip Boundaries. *Journal of Fluid Mechanics,* 418, 189-212

IOC, SCOR and IAPSO, (2010). *The International Thermodynamic Equation of Seawater – 2010: Calculation and Use of Thermodynamic Properties*, Intergovernmental Oceanographic Commission, Manuals and Guides No. 56, UNESCO (English), 196.

Luque, F.R. & Van Beek, R. (1976). Erosion and Transport of Bed-Load Sediment. *Journal of Hydraulic Research,* 14(2), 127-144.

Meneveau, C., Lund, T.S. & Cabot, W.H. (1996). A Lagrangian Dynamic Subgrid-Scale Model of Turbulence. *Journal of Fluid Mechanics,* 319, 353-385.

Necker, F., Härtel, C., Kleiser, L. & Meiburg, E. (2002). High-Resolution Simulations of Particle-Driven Gravity Currents. *International Journal of Multiphase Flow,* 28, 279–300.

Nogueira, H.I., Adduce, C., Alves, E. & Franca, M.J. (2013). Analysis of Lock-Exchange Gravity Currents over Smooth and Rough Beds. *Journal of hydraulic Research,* 51(4), 417-431.

Ooi, S.K., Constantinescu, G. & Weber, L. (2009). Numerical Simulations of Lock-Exchange Compositional Gravity Current. *Journal of Fluid Mechanics,* 635.

Ottolenghi, L., Adduce, C., Inghilesi, R., Roman, F. & Armenio, V. (2016). Mixing in Lock-Release Gravity Currents Propagating Up a Slope. *Physics of Fluids,* 28(5), 056604.

Parsons, J.D., & García, M.H. (1998). Similarity of Gravity Current Fronts. *Physics of Fluids,* 10(12), 3209-3213.

Shields, A. (1936). *Anwendung der Ähnlichkeitsmechanik und der Turbulenzforschung auf die Geschiebebewegung*. Mitteilung der Preußischen Versuchsanstalt für Wasser und Schiffsbau, Berlin, 26.

Simpson, J.E. (1997). *Gravity Currents: In the Environment and the Laboratory.* Cambridge University Press.

Theiler, Q. & Franca, M.J. (2016). Contained Density Currents with High Volume of Release. *Sedimentology,* 63(6), 1820-1842.

Tokyay, T., Constantinescu, G. & Meiburg, E. (2011). Lock-Exchange Gravity Currents with a High Volume of Release Propagating over a Periodic Array of Obstacles. *Journal of Fluid Mechanics,* 672, 570-605.

Vanoni, V. A. (1975). *Sedimentation Engineering,* ASCE Task Committee for the Preparation of the Manual on Sedimentation of the Sedimentation Committee of the Hydraulics Division.

Vinokur, M. (1983). On One-Dimensional Stretching Functions for Finite-Difference Calculations. *Journal of Computational Physics,* 50, 215

Van Rijn, Leo C. (1984). Sediment Pick-Up Functions. *Journal of Hydraulic Engineering,* 110.10, 1494-1502.

Zang, Y., Street, R.L. & Koseff, J.R. (1994). A Non-Staggered Grid, Fractional Step Method for Time-Dependent Incompressible Navier-Stokes Equations in Curvilinear Coordinates. *Journal of Computational Physics,* 114(1), 18-33.

Zanke, U.C.E. (1977). *Berechnung der Sinkgeschwindigkeiten von Sedimenten*. Mitteilungen des Franzius-Instituts für Wasserbau, Technische Universität Hannover, 46, 243.

Zordan, J., Juez, C., Schleiss, A.J. & Franca, M.J. (2017). Experimental Results on Gravity Current's Dynamic initiating Sediments Entrainment. *In IAHR 2017.*

